ARTICLE   OPEN

Thermal property and failure behaviors of Gd doped LaZrCeO coatings with feathery microstructure

Zaoyu Shen [1] ✉, Guanxi Liu[1], Limin He[1], Rende Mu[1] and Jianwei Dai[1]

LaZrCeO coatings are promising candidates to substitute Y_2O_3-stabilized ZrO_2 in advanced gas turbine engines. In this study, Gd doped LaZrCeO coatings were deposited by electron beam physical vapor deposition. This study focuses on the phase, microstructure, thermal property, and thermal durability of $(La_{1-x}Gd_x)_2(Zr_{0.7}Ce_{0.3})_2O_7$ coatings. The as-deposited coatings show relatively good thermal shock life and thermal cycling life. The broken regions are observed on the interface of thermal barrier coatings. The failure behaviors are relevant with crack evolution and thermally grown oxide growth. This study might guide the investigation of advanced coatings under high temperature.

INTRODUCTION

In recent years, the demand for advanced gas-turbines is growing along with the development of related aviation manufacturing technology. Thermal barrier coatings (TBCs) play a key role in the development of next-generation gas-turbine engines[1,2]. As we know, the efficiency and power output are related to the gas temperature of gas-turbine engines. Thus, the application of TBCs is urgently required in order to secure service life in high temperature and extreme conditions. In general, TBCs are metallic coatings + ceramic coatings duplex systems in order to provide thermal insulation to turbine blades and vane blades. Nowadays, Y_2O_3-stabilized ZrO_2 (YSZ) is already applied in gas-turbine engines that mainly include stable tetragonal prime phase[2]. Nevertheless, YSZ usually shows the low thermal durability and premature failure due to the phase instability and low sintering resistance (>1180 °C)[2].

In order to improve thermal durability, researchers have designed muti-coatings and explored novel ceramic materials[3–6]. The novel ceramic materials ($La_2Zr_2O_7$, $Gd_2Zr_2O_7$, $La_2Ce_2O_7$, $Sm_2Zr_2O_7$ and so on) have been studied to substitute YSZ[7–16]. Among these interesting ceramic materials, $La_2Zr_2O_7$ (LZ) has received much more attention owing to the lower thermal conductivity compared with YSZ[7]. To further reduce thermal conductivity, the heavy rare elements (Ce, Sm, Yb, Er) have been selected to substitute for A site or B site in LZ ceramics[8,13,17,18]. The doping of substitution elements will introduce point defects into the $La_2Zr_2O_7$ crystal, which can improve the phonon-point defect scattering leading to the reduction of thermal conductivity. On the other hand, the heavy rare elements doping in LZ also exhibit a high thermal expansion coefficient and phase stability in comparison to YSZ[19,20]. The high thermal expansion coefficient and phase stability of TBCs can alleviate residual stress and improve thermal protection ability leading to high thermal cycling life. In our previous work, $La_2(Zr_{0.7}Ce_{0.3})_2O_7$ (LZ7C3) exhibits high TEC and high thermal property[15]. However, seldom work focuses on the La site substitution (Gd doping) of LZ7C3 ceramics and their TBCs. In particular, the effects of Gd substitution on the structure, thermal conductivity, and thermal durability have yet to be studied in the literature. Furthermore, the relationship of cracks

evolution and TGO growth still remain challenging in the study of TBCs failure.

The objective of the work is to study the $(La_{1-x}Gd_x)_2(Zr_{0.7}Ce_{0.3})_2O_7$ as advanced TBCs. The $(La_{1-x}Gd_x)_2(Zr_{0.7}Ce_{0.3})_2O_7$ coatings were prepared by electron beam-physical vapor deposition. The phase, composition, and microstructure of $(La_{1-x}Gd_x)_2(Zr_{0.7}Ce_{0.3})_2O_7$ coatings were investigated by XRD, SEM, EDS, EPMA, and TEM. The relationship between cracks evolution and interface stability has been investigated in this work.

RESULTS AND DISCUSSIONS

Phase structure

As shown in XRD patterns, all the $(La_{1-x}Gd_x)_2(Zr_{0.7}Ce_{0.3})_2O_7$ coatings deposited by EB-PVD are detected by a cubic pyrochlore structure (JCPDS No.17-0450). In our previous work, the LaZrCeO coatings exhibit a cubic pyrochlore structure by EB-PVD[14–16]. In the $La_2Zr_2O_7$ phase structure, La substitution by similar lanthanides (Gd, Sm, Ce) would remain the pyrochlore structure[4,7]. The radius of La^{3+} (0.116 nm) is similar to the Gd^{3+} (0.105 nm) that is both much bigger than the radius of Zr^{2+} (0.072 nm). The ionic radius ratio of Gd^{3+}/Zr^{4+} and La^{3+}/Zr^{4+} is about 1.46 and 1.61 which is large than 1.44. Therefore, the pyrochlore typed $(La_{1-x}Gd_x)_2(Zr_{0.7}Ce_{0.3})_2O_7$ is comparatively tolerant to Gd substitution in this work.

As shown in XRD patterns, the peaks at $2\theta \approx 28.68°$, 33.26°, 47.60°, 56.50°, 59.36°, 69.72°, 77.02°, 79.42°, and 88.82° could be indexed to the (222), (400), (440), (622), (444), (800), (622), (840), and (844) plane of $La_2Zr_2O_7$, respectively. Furthermore, the peaks at $2\theta \approx 36.32°$ and 43.54° are indexed to the (331) and (511) that are the characteristic peak of pyrochlore structure[4]. The peaks position of $(La_{1-x}Gd_x)_2(Zr_{0.7}Ce_{0.3})_2O_7$ is not changed compared to LaZrCeO, indicating that the Gd substitution into the La lattice does not change the crystal structure. Furthermore, according to the peaks intensity, the peaks at 28.68° are the growth direction of $(La_{1-x}Gd_x)_2(Zr_{0.7}Ce_{0.3})_2O_7$ coatings. That means, the growth orientation of $(La_{1-x}Gd_x)_2(Zr_{0.7}Ce_{0.3})_2O_7$ occurs in the (222) crystal direction (Fig. 1).

[1]Key Laboratory of Advanced Corrosion and Protection for Aviation Materials, Beijing Institute of Aeronautical Materials, Aero Engine Corporation of China, 100095 Beijing, PR China. ✉email: shenzaoyu@163.com

Microstructure

The cross-section morphology of the coatings is shown in Fig. 2a. Three layers (L7G3Z7C3 + YSZ + NiCoCrAlYHf) are clearly shown in the TBCs system. The thickness of the three layers is 80–90, 85–95, and 50–60 µm from top to bottom, respectively. The cross-section morphology of top and middle coatings is columnar structure due to the high vacuum process of EB-PVD, while the bottom layer is equiaxed structure due to the PVD process[1–4]. The interface microstructure between the top layer and the middle layer is observed by clearly SEM image (Fig. 2b). The columnar structure continuously grows and extends between two layers. The interface of the two layers also shows relatively smooth bonding.

Due to the deposition sequence, the top layer might be L7G3Z7C3 coatings and the middle layer might be YSZ coatings, while the bottom might be NiCoCrAlYHf coatings. As shown in Fig. 2c, the existence and distribution of La, Gd, Zr, and Ce have been mainly detected in the top layer corresponding to the L7G3Z7C3. Furthermore, the existence and distribution of Zr and Y have been mainly detected in the middle layer corresponding to the YSZ.
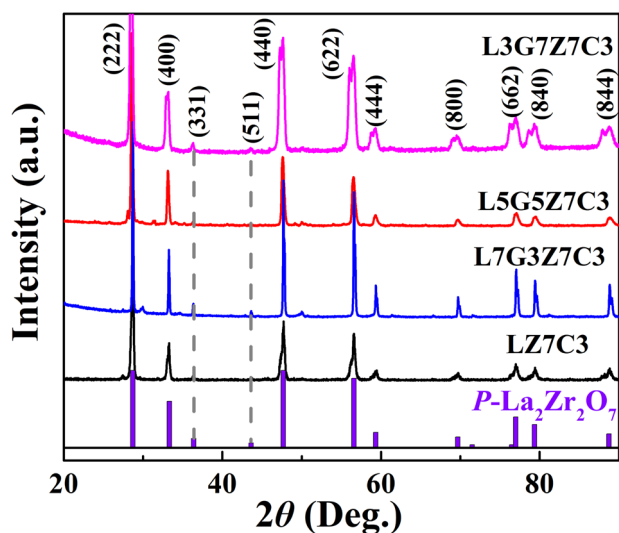
Furthermore, it also reveals the co-existence of Ni, Co, Cr, Al, Y, and Hf could be detected in the bottom layer corresponding to the NiCoCrAlYHf. The EDS line scanning of Zr element confirms the existence of three layers (L7G3Z7C3 + YSZ + NiCoCrAlYHf) in TBCs system. That is to say, the element distribution is relatively uniform in TBCs system.

As we know, the high-angle annular dark-field (HAADF) is a method for investigating hierarchical microstructure with different atom sensitivity. The method of HAADF detector forms a Z-contrast image. The intensity of the image contributed by different atoms is approximately proportional to Z^2 (Z is the atomic number), with intensity being greater for heavier atoms and depending also on the number of atoms in a column[21,22]. As shown in Fig. 3, it clearly shows the microstructure of L7G3Z7C3 coatings. Figure 3a is the HAADF image that clearly shows the obvious feathery microstructure. The feathery microstructure is mainly composited of nano-sized inter-gaps and pores which run normal to the ceramic-metal interface due to the EB-PVD process. Figure 3a is the HAADF image that clearly shows the obvious feathery microstructure. Furthermore, the HAADF indicates the uniform distribution of four elements (La, Gd, Zr, Ce, and O) in L7G3Z7C3 coatings. Figure 3b is the high-resolution transmission electron microscope (HRTEM) image of L7G3Z7C3 coatings. The value of lattice space (0.265 nm and 0.192 nm) can be observed in the L7G3Z7C3 coatings, which correspond to (400) and (440) of the $La_2Zr_2O_7$. Furthermore, the corresponding SEAD pattern obtained from the feathery microstructure indicates that the L7G3Z7C3 coatings are mainly composited of the pyrochlore structure of $La_2Zr_2O_7$ (Fig. 3c). In general, the feathery structure has been successfully obtained due to the EB-PVD deposition which might play a key role in the improvement of strain tolerance[1,2].

Thermal property

According to the analyses above, it could be expected that $(La_{1-x}Gd_x)_2(Zr_{0.7}Ce_{0.3})_2O_7$ coatings might be used as TBCs under high temperature. Figure 4 shows the thermal durability of $(La_{1-x}Gd_x)_2(Zr_{0.7}Ce_{0.3})_2O_7$ coatings under the same condition (1373 K 5 min heating/5 min cooling or 55 heating/5 min cooling). Both thermal shock and cycling life of L7G3Z7C3 coatings exhibit the highest life (4613 cycles and 602 h) than that of L5G5Z7C3 TBCs and L3G7Z7C3 TBCs. The thermal shock and cycling life of L7G3Z7C3 coatings has exceeded the majority value of advanced ceramic coatings in TBCs field[2,10,11,17–20]. The enhanced thermal

Fig. 1 XRD patterns of $(La_{1-x}Gd_x)_2(Zr_{0.7}Ce_{0.3})_2O_7$ coatings. All the $(La_{1-x}Gd_x)_2(Zr_{0.7}Ce_{0.3})_2O_7$ coatings were deposited by EB-PVD under same condition.
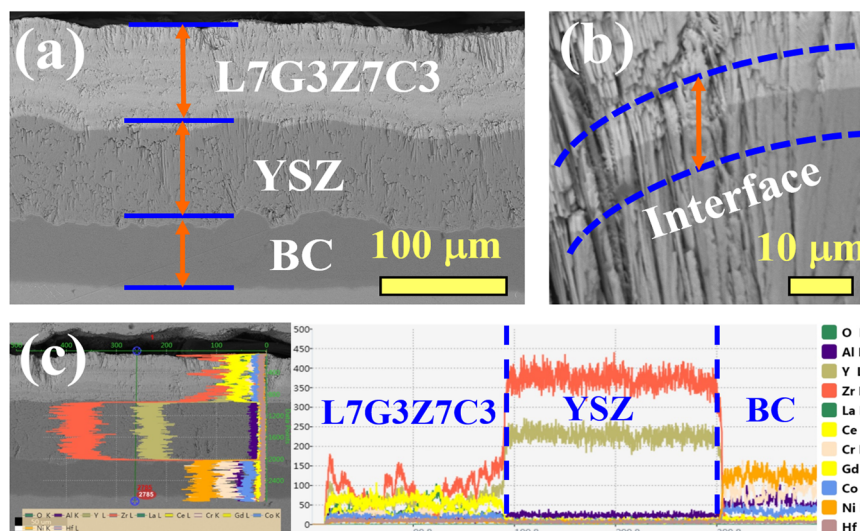

Fig. 2 Microstructure of as-deposited L7G3Z7C3/YSZ/BC TBCs system. a cross-section morphology, **b** interface microstructure, and **c** EDS line scanning.
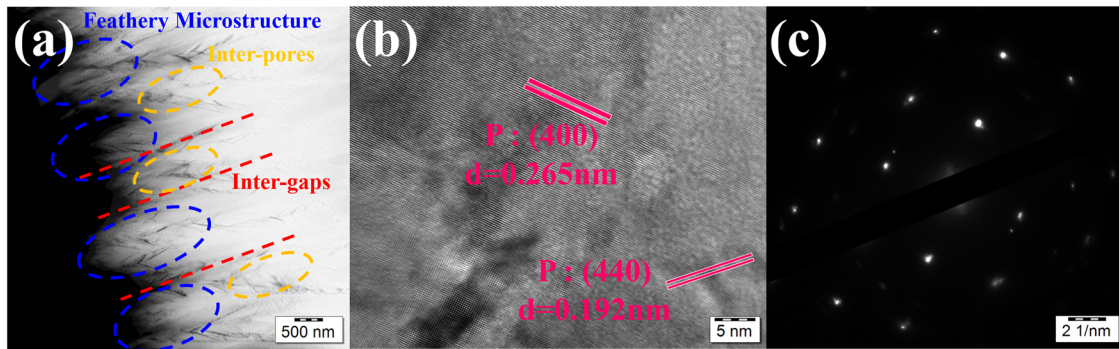
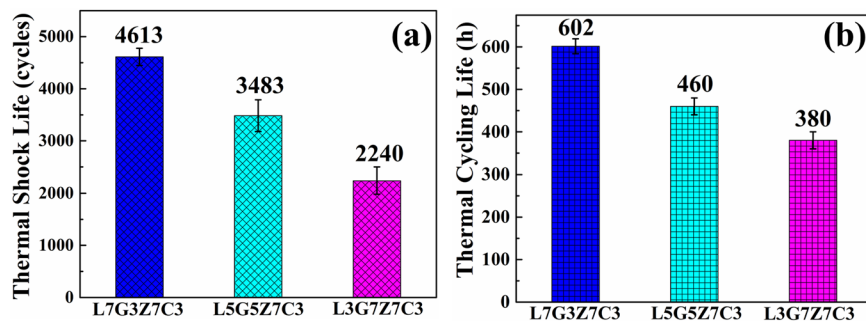**Fig. 3 Microstructure of L7G3Z7C3 coatings. a** HADDF, **b** HRTEM, and **c** SAED image.

Fig. 4 Thermal durability of the (La$_{1-x}$Gd$_x$)$_2$(Zr$_{0.7}$Ce$_{0.3}$)$_2$O$_7$ coatings. a Thermal shock life and **b** Thermal cycling life.
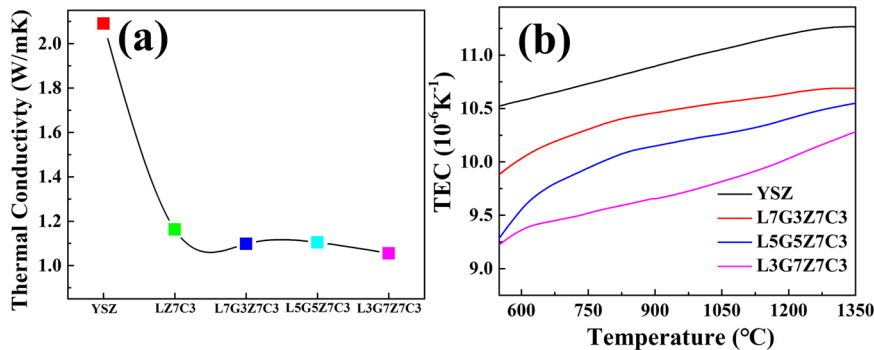
Fig. 5 Thermal property of (La$_{1-x}$Gd$_x$)$_2$(Zr$_{0.7}$Ce$_{0.3}$)$_2$O$_7$ and YSZ ceramics. a thermal conductivity at 1200 °C and **b** thermal expansion coefficient.

durability indicates the key effect of Gd content, that is, the added Gd component leads to the improvement of thermal protection.

As shown in Fig. 5a, the thermal conductivity of (La$_{1-x}$Gd$_x$)$_2$(Zr$_{0.7}$Ce$_{0.3}$)$_2$O$_7$ and YSZ ceramics has been measured at 1200 °C. In total, the thermal conductivity of (La$_{1-x}$Gd$_x$)$_2$(Zr$_{0.7}$Ce$_{0.3}$)$_2$O$_7$ is about 50% lower than YSZ. Furthermore, it also indicates that the Gd content in LaZrCeO has an effect on the thermal conductivity. When the Gd is introduced into the (La$_{1-x}$Gd$_x$)$_2$(Zr$_{0.7}$Ce$_{0.3}$)$_2$O$_7$ ceramics, the value of thermal conductivity would decrease with the improvement of Gd content. The Gd substitution would introduce more point defects into LaZrCeO, which can further improve the phonon-point defect scattering leading to the reduction of thermal conductivity[23]. In particular, the L3G7Z7C3 ceramics exhibits the lowest value of thermal conductivity (1.05 W/mK) compared with that of L5G5Z7C3 and L7G3Z7C3. As we know, the low thermal conductivity would provide a relatively good thermal protection to YSZ, BC, and further to the substrate, which might further lead to the thermal durability extension of TBCs. As shown in Fig. 5b, the TEC of YSZ and (La$_{1-x}$Gd$_x$)$_2$(Zr$_{0.7}$Ce$_{0.3}$)$_2$O$_7$ ceramics has been

detected in the range of 550–1350 °C. The L7G3Z7C3 ceramics exhibits the highest TEC (9.88–10.69*10^{-6} K^{-1}) among all (La$_{1-x}$Gd$_x$)$_2$(Zr$_{0.7}$Ce$_{0.3}$)$_2$O$_7$ ceramics. Generally, the high value of TEC would provide a relatively good thermal-mechanical protection to TBCs system. The improvement of TEC attributes to the ionic radius/ cationic field strength of Gd introduction[24,25]. Thus, the high TEC of L7G3Z7C3 would provide better thermal-mechanical compatibility to YSZ layer, TGO layer, BC layer, and Ni-based superalloy leading to the longest thermal durability[26–28]. In addition, large rare-earth ions in Ln$_2$Zr$_2$O$_7$ (Ln=Nd, Sm, Gd) can lead to a stable pyrochlore structure up to 1700 K[4,7,23]. Thus, the Gd substitution in La$_2$Zr$_2$O$_7$ might lead to a stable pyrochlore structure under high temperature. The stable effect of Gd content could further introduce the relatively complex and large defects that can improve the sintering resistance[4,7]. In particular, the coatings are formed by vapor condensation and are characterized by a columnar microstructure with a feathery structure containing nano-sized inter-gaps and pores which might improve the strain tolerance, impart in-plane compliance, and thermal shock resistance leading to the high thermal durability[1,2,29]. Furthermore,
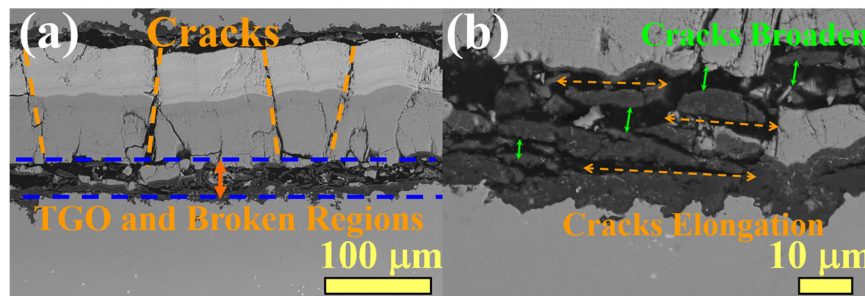
Fig. 6 **Cross-section morphology after thermal cycling test. a** TBCs and **b** TGO layer.
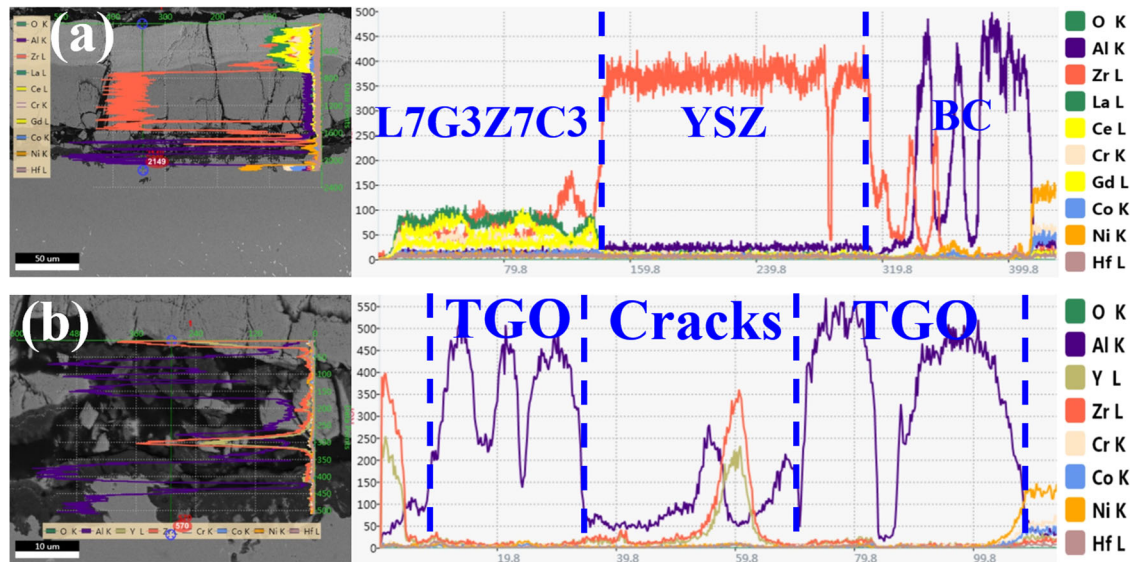

Fig. 7 **EDS line scanning after thermal cycling test. a** TBCs and **b** TGO layer.

the formation of double-layer coatings of L7G3Z7C3/YSZ might benefit from the higher fracture toughness of the YSZ middle layer coatings, further providing good adhesion of the TBCs system. In general, the improvement of TEC, the feathery structure with nano-sized inter-gaps and pores, and the stable effect of Gd substitution lead to good thermal durability.

Failure behavior

To clearly elucidate the high thermal durability and intrinsic failure behavior of TBCs, the cross-section of TBCs and TGO are investigated after the thermal cycling test. As we know, TGO growth and cracks evolution strongly influence intrinsic failure behavior. Figure 6a shows the evolution of the crack in which the vertical cracks primarily occur on the ceramic layer. Because of the TEC mismatch among L7G3Z7C3, YSZ and NiCoCrAlYHf, the vertical cracks have penetrated in L7G3Z7C3 layer and YSZ layer, and further extended to NiCoCrAlYHf layer. With the heating-cooling process of the thermal cycling test, the length and width of vertical cracks also increase in the TGO layer under high temperature. Due to the TEC mismatch among YSZ, TGO, and NiCoCrAlYHf layer, the mainly broken regions are observed on TGO interface after the thermal cycling test. Further observation indicates that the cracks coalesce into a separation zone leading to the damage of the connection between YSZ and TGO layer (Fig. 6b). At the end of the thermal test, the vertical and horizontal cracks have already extended and coalesced in TGO layer. The massive vertical and horizontal cracks in TGO would lead to the instability of TBCs system[30–34]. The vertical and horizontal cracks might also reduce the strain tolerance in the TBCs system[35–37].

To further study the element evolution, the EDS analyses of TBCs and TGO is detected after the thermal test. Figure 7a shows the coexistence of La, Gd, Zr, Ce, and O which has been mainly detected in L7G3Z7C3 coatings. The element content of coatings shows relatively stable and uniform distribution under high temperature. As shown in Fig. 7b, the existence of Al and O is also relatively uniform distribution in TGO layer. The violet peak is the position of Al_2O_3, while the violet valley is the position of cracks. It indicates that the cracks have spread throughout TGO layer. To further clearly elucidate the thermal durability and failure behavior of TBCs at 1100 °C, the cross-section morphology and EPMA mapping images are detected after the thermal cycling test (Fig. 8). As shown in Fig. 8a, the thickness of TGO layer is about 15 μm. The bright point in the TGO layer might be the element enrichment zone. As shown in Fig. 8b–h, EPMA mapping images correspond to Al, O, Zr, Ni, Co, Y, and Hf element, respectively. As shown in Fig. 8b, c, the Al and O element are detected in TGO layer corresponding to the chemical composition of Al_2O_3. The dark zone is the position of cracks. It indicates that the vertical and horizontal cracks both have spread throughout TGO layer. As shown in Fig. 8e, the EMPA images clearly show that the Ni element has been partly diffused and concentrated in the TGO layer. As shown in Fig. 8f–h, the EMPA images show the Y and Hf rich zones. It indicates that the Y and Hf two elements are also partly diffused and concentrated in TGO layer. These results indicate that the Y-Hf-O oxides have grown and formed in TGO layer. As thermal cycling proceeds, the TEC and thermal-mechanical property mismatch among Y-Hf-O oxides, Al_2O_3 and BC would lead to the growth and formation of instabilities[32–34]. In addition, the diffusion of BC element might also accelerate the

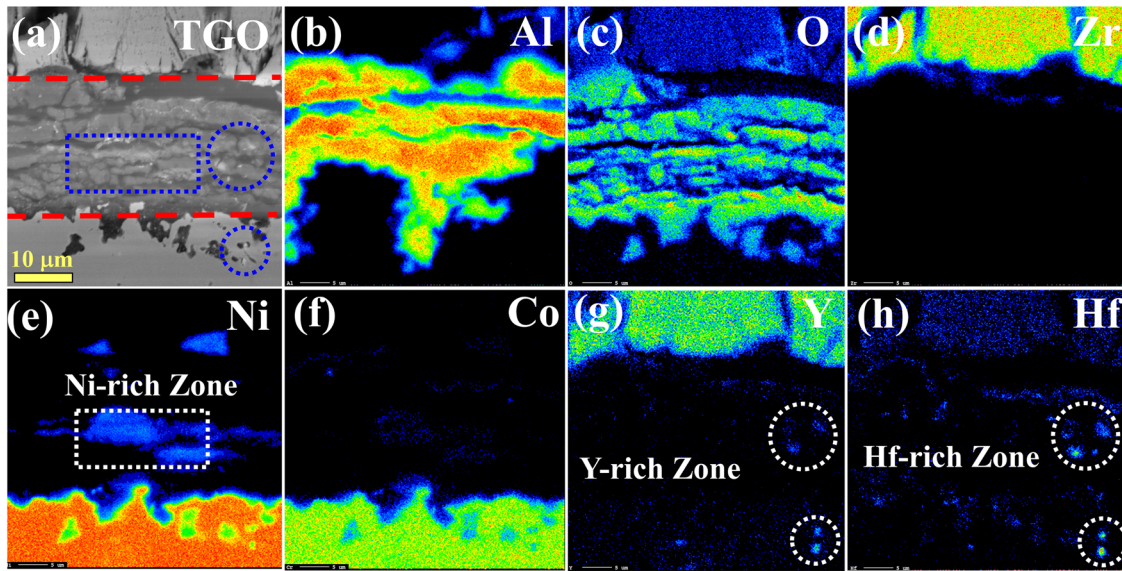**Fig. 8 EPMA mapping images of TBCs after thermal cycling test. a** cross-section morphology, **b** Al, **c** O, **d** Zr, **e** Ni, **f** Co, **g** Y, and **h** Hf.

growth and formation of Al_2O_3 and extension and elongation of cracks leading to the failure of TBCs[38–41]. In general, TGO and crack evolution play a key role in the failure mechanism. This work might provide some experience to study other advanced TBCs under high temperature.

In summary, the $(La_{1-x}Gd_x)_2(Zr_{0.7}Ce_{0.3})_2O_7$ coatings are deposited by EB-PVD. The $(La_{1-x}Gd_x)_2(Zr_{0.7}Ce_{0.3})_2O_7$ coatings mainly exhibit a pyrochlore structure. The coatings are composed of $(La_{1-x}Gd_x)_2(Zr_{0.7}Ce_{0.3})_2O_7$, YSZ, and NiCoCrAlYHf. The $(La_{1-x}Gd_x)_2(Zr_{0.7}Ce_{0.3})_2O_7$ coatings exhibit a relatively high thermal durability due to the improvement of TEC, the formation of feathery structure, and double-layer coatings, and the stable effect of Gd substitution. The massive vertical and horizontal cracks in TGO lead to the instability of TBCs system. TGO and crack evolution play a key role in the failure mechanism of TBCs. The $(La_{1-x}Gd_x)_2(Zr_{0.7}Ce_{0.3})_2O_7$ coatings might be one advanced TBCs material.

METHODS

Deposition of TBCs

The substrate material was Ni-based superalloy ($30.0 \times 10.0 \times 1.0$ mm). The composition of substrate material is 12.5 wt.% Co, 6.3 wt.% W and Al, 5.8 wt.% Ta and Cr, 2.2 wt.% Re, 1.3 wt.% Mo and Ni as balance. The NiCoCrAlYHf was selected as bond coatings and deposited by physical vapor deposition technology (PVD, A-1000 Unit, Russia). In the deposition process, the current was 650 A. The deposition process was completed below 1×10^{-2} Pa. The deposition rate of NiCoCrAlYHf is about 0.25 μm/min. Then, the substrate material with NiCoCrAlYHf was annealed under a high vacuum ($<1 \times 10^{-}$ Pa) at $870 \pm 10\,°C$ for 3 h to enhance bond strength. The phase of NiCoCrAlYHf coatings is β phase and γ' phase.

The raw materials (>99.99%) of La_2O_3, Gd_2O_3, ZrO_2 and CeO_2 were reacted at $1500\,°C$ for 24 h by solid-state reaction. The L3G7Z7C3, L5G5Z7C3, and L7G3Z7C3 are short for $(La_{1-x}Gd_x)_2(Zr_{0.7}Ce_{0.3})_2O_7$ (x = 0.3, 0.5, 0.7). The composition of YSZ was 8.0 at.% Y, 92.0 at.% Zr and O as balance. The $(La_{1-x}Gd_x)_2(Zr_{0.7}Ce_{0.3})_2O_7$ and YSZ were used as ceramic coatings and deposited by EB-PVD (UE-207S, Ukraine). The chamber pressure was kept in a high vacuum condition (below 1×10^{-2} Pa). The deposition rate of YSZ is about 3.0 μm/min, while the deposition rate of $(La_{1-x}Gd_x)_2(Zr_{0.7}Ce_{0.3})_2O_7$ is about 2.5 ± 0.5 μm/min. The thickness of L3G7Z7C3, L5G5Z7C3, and L7G3Z7C3 is about 80–100 μm. The thickness of YSZ is about 80–100 μm. The thickness of NiCoCrAlYHf, YSZ, and $(La_{1-x}Gd_x)_2(Zr_{0.7}Ce_{0.3})_2O_7$ is obtained by our previous work and the open literature[2,9–12].

Characterizations

The phases of coatings were detected by X-ray diffraction (XRD, D8 Advance). The composition and microstructure of coatings were analyzed by SEM (FEI-Quanta 600), EDS (Oxford INCAx-sight 6427), and TEM (JEM-2100F). The element mapping images of coatings were detected by FE-EPMA (JXA-8100). The specific heat capacities of $(La_{1-x}Gd_x)_2(Zr_{0.7}Ce_{0.3})_2O_7$ are calculated by Neumann-Kopprule[42]. The thermal conductivity of $(La_{1-x}Gd_x)_2(Zr_{0.7}Ce_{0.3})_2O_7$ is calculated by the formula: $\lambda = \rho \times \alpha \times Cp$. The thermal expansion coefficient of ceramics was detected by Netzsch DIL 402C. In the thermal durability test, the coatings were heated at 1373 K for 55 min or 5 min in the furnace. Then, the coatings were cooled by air for 5 min. The temperature of TBCs surface is below 300 °C at the end of each cycle. When the broken area excess 10%, the cycles were regarded as thermal durability.

REFERENCES

1. Padture, N. P., Gell, M. & Jordan, E. H. Thermal barrier coatings for gas-turbine engine applications. *Science* **296**, 280–284 (2002).
2. Clarke, D. R., Oechsner, M. & Padture, N. P. Thermal-barrier coatings for more efficient gas-turbine engines. *MRS Bull.* **37**, 891–898 (2012).
3. Levi, C. G. Emerging materials and processes for thermal barrier systems. *Curr. Opin. Solid State Mater. Sci.* **8**, 77–91 (2002).
4. Vaßen, R., Jarligo, M. O., Steinke, T. & Mack, D. E. Overview on advanced thermal barrier coatings. *Surf. Coat. Technol.* **205**, 938–942 (2010).
5. Sampath, S., Schulz, U., Jarligo, M. O. & Kuroda, S. Processing science of advanced thermal-barrier systems. *MRS Bull.* **37**, 903–910 (2012).
6. Pollock, T. M., Lipkin, D. M. & Hemker, K. J. Multifunctional coating interlayers for thermal-barrier systems. *MRS Bull.* **37**, 923–931 (2012).
7. Zhao, M. et al. Defect engineering in development of low thermal conductivity materials: a review,. *J. Eur. Ceram. Soc.* **37**, 1–13 (2017).
8. Dong, S. J. et al. Thermal radiation and cycling properties of (Ca, Fe) or (Sr, Mn) co-doped $La_2Ce_2O_7$ coatings. *J. Eur. Ceram. Soc.* **40**, 2020–2029 (2020).
9. Shen, Z. Y. et al. Effects of Er stabilization on thermal property and failure behavior of $Gd_2Zr_2O_7$ thermal barrier coatings. *Corros. Sci.* **185**, 109418 (2021).
10. Mahade, S. et al. Functional performance of $Gd_2Zr_2O_7$/YSZ multi-layered thermal barrier coatings deposited by suspension plasma spray. *Surf. Coat. Technol.* **318**, 208–216 (2017).

11. Gok, M. G. & Goller, G. Production and characterization of GZ/CYSZ alternative thermal barrier coatings with multilayered and functionally graded designs. *J. Eur. Ceram. Soc.* **36**, 1755–1764 (2016).

12. Shen, Z. Y. et al. LaGdZrO/YSZ thermal barrier coatings by EB-PVD: Microstructure, thermal properties and failure mechanism. *Chem. Eng. J. Adv.* **5**, 100073 (2021).

13. Hong, Q. J., Ushakov, S. V., Navrotsky, A. & Walle, A. Combined computational and experimental investigation of the refractory properties of La$_2$Zr$_2$O$_7$. *Acta Mater.* **84**, 275–282 (2015).

14. Shen, Z. Y., He, L. M., Xu, Z. H., Mu, R. D. & Huang, G. H. Morphological evolution and failure of LZC/YSZ DCL TBCs by electron beam-physical vapor deposition. *Materialia* **4**, 340–347 (2018).

15. Shen, Z. Y., He, L. M., Xu, Z. H., Mu, R. D. & Huang, G. H. LZC/YSZ DCL TBCs by EB-PVD: microstructure, low thermal conductivity and high thermal cycling life. *J. Eur. Ceram. Soc.* **39**, 1443–1450 (2019).

16. Shen, Z. Y., He, L. M., Mu, R. D., Xu, Z. H. & Huang, G. H. Effects of gradient transitional layer on thermal cycling life and failure of LaZrCeO/YSZ thermal barrier coatings. *Corros. Sci.* **163**, 108224 (2020).

17. Wang, X. Z., Guo, L., Zhang, H. L., Gong, S. K. & Guo, H. B. Structural evolution and thermal conductivities of (Gd$_{1-x}$Yb$_x$)$_2$Zr$_2$O$_7$ (*x* = 0, 0.02, 0.04, 0.06, 0.08, 0.1) ceramics for thermal barrier coatings. *Ceram. Inter.* **41**, 12621–12625 (2015).

18. Wan, C. L., Qu, Z. X., Du, A. & Pan, W. Influence of B site substituent Ti on the structure and thermophysical properties of A$_2$B$_2$O$_7$-type pyrochlore Gd$_2$Zr$_2$O$_7$. *Acta Mater.* **57**, 4782–4789 (2009).

19. Bahamirian, M., Hadavi, S. M. M., Farvizi, M., Rahimipour, M. R. & Keyvani, A. Phase stability of ZrO$_2$ 9.5Y$_2$O$_3$ 5.6Yb$_2$O$_3$ 5.2Gd$_2$O$_3$ compound at 1100 °C and 1300 °C for advanced TBC applications. *Ceram. Int.* **45**, 7344–7350 (2019).

20. Song, D. et al. Hot-corrosion resistance and phase stability of Yb$_2$O$_3$-Gd$_2$O$_3$-Y$_2$O$_3$ costabilized zirconia-based thermal barrier coatings against Na$_2$SO$_4$+V$_2$O$_5$ molten salts. *Surf. Coat. Technol.* **400**, 126 (2020).

21. Ortalan, V., Uzun, A., Gates, B. C. & Browning, N. D. Browning. Towards full-structure determination of bimetallic nanoparticles with an aberration-corrected electron microscope. *Nat. Nanotechol.* **5**, 843–847 (2010).

22. Muller, D. A. Structure and bonding at the atomic scale by scanning transmission electron microscopy. *Nat. Mater.* **8**, 263–270 (2009).

23. Pan, W., Phillpot, S. R., Wan, C. L., Chernatynskiy, A. & Qu, Z. X. Low thermal conductivity oxides. *MRS Bull.* **37**, 917–922 (2012).

24. Shen, Z. Y. et al. Effects of Gd content on the phase structure and thermal property of (La$_{1-x}$Gd$_x$)$_2$(Zr$_{0.7}$Ce$_{0.3}$)$_2$O$_7$ ceramics. *Open Ceram.* **7**, 100144 (2021).

25. Shen, Z. Y. et al. GdYbZrO thermal barrier coatings by EB-PVD: Phase, microstructure, thermal properties and failure. *Surf. Interfaces* **24**, 101125 (2021).

26. Malzbender, J. & De With, G. Energy dissipation, fracture toughness and the indentation load-displacement curve of coated materials. *Surf. Coat. Technol.* **135**, 60–68 (2000).

27. Zhang, X. C., Watanabe, M. & Kuroda, S. Effects of processing conditions on the mechanical properties and deformation behaviors of plasma-sprayed thermal barrier coatings: evaluation of residual stresses and mechanical properties of thermal barrier coatings on the basis of in situ curvature measurement under a wide range of spray parameters. *Acta Mater.* **61**, 1037–1047 (2013).

28. Zhou, F. F. et al. Bonding strength and thermal conductivity of novel nanostructured La$_2$(Zr$_{0.75}$Ce$_{0.25}$)$_2$O$_7$/8YSZ coatings. *Appl. Surf. Sci.* **481**, 460–465 (2019).

29. Vaßen, R., Kagawa, Y., Subramanian, R., Zombo, P. & Zhu, D. M. Testing and evaluation of thermal-barrier coatings. *MRS Bull.* **37**, 911–916 (2012).

30. Liu, D., Rinaldi, C. & Flewitt, P. E. J. Effect of substrate curvature on the evolution of microstructure and residual stresses in EBPVD-TBC. *J. Eur. Ceram. Soc.* **35**, 2563–2575 (2015).

31. Jonnalagadda, K. P. et al. A study of damage evolution in high purity nano TBCs during thermal cycling: a fracture mechanics based modelling approach. *J. Eur. Ceram. Soc.* **37**, 2889–2899 (2017).

32. Chen, Y., Zhao, X. F. & Xiao., P. Effect of microstructure on early oxidation of MCrAlY coatings. *Acta Mater.* **159**, 150–162. (2018).

33. Chen, Y. et al. A mechanistic understanding on rumpling of a NiCoCrAlY bond coat for thermal barrier coating applications. *Acta Mater.* **128**, 31–42 (2017).

34. Yang, L. X. et al. High temperature stress and its influence on surface rumpling in NiCoCrAlY bond coat,. *Acta Mater.* **139**, 122–137 (2017).

35. Tolpygo, V. K., Murphy, K. S. & Clarke, D. R. Effect of Hf, Y and C in the underlying superalloy on the rumpling of diffusion aluminide coatings. *Acta Mater.* **56**, 489–499 (2008).

36. Evans, A. G., Mumm, D. R., Hutchinson, J. W., Meier, G. H. & Pettit, F. S. Mechanisms controlling the curability of thermal barrier coatings. *Prog. Mater. Sci.* **46**, 505–553 (2001).

37. Ghadami, F., Aghdam, A. S. R. & Ghadami, S. Microstructural characteristics and oxidation behavior of the modified MCrAlX coatings: a critical review. *Vacuum* **185**, 109980 (2021).

38. Evans, A. G., Clarke, D. R. & Levi, C. G. The influence of oxides on the performance of advanced gas turbines. *J. Eur. Ceram. Soc.* **28**, 1405–1419 (2008).

39. Balint, D. S. et al. Evans. Anisotropic TGO rumpling in EB-PVD thermal barrier coatings under in-phase thermomechanical loading. *Acta Mater.* **59**, 2544–2555 (2011).

40. Shen, Z. Y., He, L. M., Xu, Z. H., Mu, R. D. & Huang, G. H. Rare earth oxides stabilized La$_2$Zr$_2$O$_7$ TBCs: EB-PVD, thermal conductivity and thermal cycling life. *Surf. Coat. Technol.* **357**, 427–432 (2019).

41. Zhen, Z. et al. Phase stability, thermo-physical property and thermal cycling durability of Yb$_2$O$_3$ doped Gd$_2$Zr$_2$O$_7$ novel thermal barrier coatings. *Ceram. Int.* **48**, 2585–2594 (2022).

42. Kubaschewski, O., Alock, C. B. & Spencer, P. J. *Materials Thermochemistry* 6th edn., 254 (Academic, 1993).

AUTHOR CONTRIBUTIONS
Z.S.: Conceptualization, Methodology, Funding, Writing—Original Draft. G.L.: Data Curation, Formal Analysis, Writing—Original Draft. L.H.: Writing—Review and Editing, Resources, Investigation, Visualization. R.M.: Validation, Resources, Investigation, Data Curation. J.D.: Validation, Investigation.

COMPETING INTERESTS
The authors declare no competing interests.

ADDITIONAL INFORMATION
Correspondence and requests for materials should be addressed to Zaoyu Shen.

Reprints and permission information is available at http://www.nature.com/reprints

Publisher's note Springer Nature remains neutral with regard to jurisdictional claims in published maps and institutional affiliations.